

Article

Spatial Evolution of Skewness and Kurtosis of Unidirectional Extreme Waves Propagating over a Sloping Beach

Iskander Abroug , Reine Matar and Nizar Abcha * 

Normandie Université, UNICAEN, UNIROUEN, CNRS, UMR 6143 M2C, 14000 Caen, France

* Correspondence: nizar.abcha@unicaen.fr

Abstract: The understanding of the occurrence of extreme waves is crucial to simulate the growth of waves in coastal regions. Laboratory experiments were performed to study the spatial evolution of the statistics of group-focused waves that have a relatively broad-banded spectra propagating from intermediate water depth to shallow regions. Breaking waves with different spectral types, i.e., spectral bandwidths and wave nonlinearities, were generated in a wave flume using the dispersive focusing technique. The non-Gaussian behavior of the considered wave trains was demonstrated by the means of the skewness and kurtosis parameters estimated from a time series and was compared with the second-order theory. The skewness and kurtosis parameters were found to have an increasing trend during the focusing process. During both the downstream wave breaking and defocusing process, the wave train dispersed again and became less steep. As a result, both skewness and kurtosis almost returned to their initial values. This behavior is clearer for narrower wave train spectra. Additionally, the learning algorithm multilayer perceptron (MLP) was used to predict the spatial evolution of kurtosis. The predicted results are in satisfactory agreement with experimental findings.



Citation: Abroug, I.; Matar, R.; Abcha, N. Spatial Evolution of Skewness and Kurtosis of Unidirectional Extreme Waves Propagating over a Sloping Beach. *J. Mar. Sci. Eng.* **2022**, *10*, 1475. <https://doi.org/10.3390/jmse10101475>

Academic Editors: Eugen Rusu and Christian Kharif

Received: 5 September 2022

Accepted: 9 October 2022

Published: 11 October 2022

Publisher's Note: MDPI stays neutral with regard to jurisdictional claims in published maps and institutional affiliations.



Copyright: © 2022 by the authors. Licensee MDPI, Basel, Switzerland. This article is an open access article distributed under the terms and conditions of the Creative Commons Attribution (CC BY) license (<https://creativecommons.org/licenses/by/4.0/>).

Keywords: skewness; kurtosis; JONSWAP; Pierson–Moskowitz; wave train; MLP model

1. Introduction

Extreme waves represent a serious problem in coastal engineering. An accurate description of the statistics of free surface elevation can improve our understanding of the propagation of large, steep waves in shallow regions and, consequently, enhance safety in coastal areas. Bitner [1] was a pioneer in the investigation of the statistics of irregular waves propagating toward a decreasing depth via field experiments. There are several mechanisms that can lead to the formation of extreme waves and, subsequently, to different shapes in the probability of the occurrence of wave heights. These mechanisms are extensively discussed in [2], while the topic of our paper is restricted to one of the well-known mechanisms of extreme wave generation, which is dispersive focusing [3–6]. The identification of a wave train, as a freak wave train, is made according to a criterion, and the one given by [7], who proposed the amplification index, $AI = H_{max}/H_s > 2$, is adopted in the present study. The parameter H_s represents the significant wave height and H_{max} is the maximum wave height, both calculated from the time series.

Using full-scale data is the best approach to investigating the statistics related to extreme waves, but the availability of such data is limited, and these data cannot be used to study the direct effect of changing a specific parameter. Numerical models often complement and expand laboratory or field studies. Despite the recent advances in the computational power in CFD models (e.g., Open-source OpenFOAM), simpler models with more computationally efficient solvers, such as FUNWAVE 2.0 used in [8,9] (based on Boussinesq approximations), are better suited to gather data from various sea states propagating in various topographies. Thus, controlled physical tests will complement findings related to the context of extreme wave formation and might also form a good basis

for testing numerical models. Wave characteristics in wave flumes have been extensively studied [10–14]. However, wave properties of extreme waves in shallow waters still require further verification, since the propagation of steep travelling wave trains include complex physical processes, such as energy transfer, nonlinear wave–wave interactions and wave breaking [15,16]. In a Gaussian sea state, the statistics of the free surface elevation can be described by its mean and variance. When waves propagate in shallow water regions and coastal areas, the sea state becomes non-Gaussian and nonlinearities are stronger. Consequently, higher-order moments can be used in order to characterize nonlinear effects. Third- and fourth-order moments, i.e., skewness λ_3 and kurtosis λ_4 , are used to measure the deviation from the Gaussian process [17]. Quantitatively, λ_3 characterizes the vertical asymmetry of the wave profile, and λ_4 reflects the peakedness and the increase in the crest to trough amplitude.

The two form parameters, skewness and kurtosis, were investigated in several studies in the case of irregular waves [17–20]. Kashima et al. [20] studied the spatial evolution of these two parameters in the case of JONSWAP random waves propagating from deep water to shallow water regions. They showed that there is no link between the skewness and kurtosis in deep water. However, [21] found that kurtosis depends on the square of skewness (i.e., $\lambda_4 = 3 + 3\lambda_3^2$). Bitner-Gregersen and Gramstad [22] proposed a spatial relationship (a second-order polynomial) between the kurtosis and skewness in the case of unidirectional JONSWAP deep-water random waves simulated using the Higher-Order Spectral Method (HOSM). In shallow regions, [20] demonstrated experimentally that there is a clear link between the two parameters regardless of the incident wave conditions. When the JONSWAP wave propagates in shallow water regions, both parameters increase and reach their maximum magnitude just prior to breaking. These results are consistent with field observations made by [1]. Recently, a similar experimental study was carried out in [23]. the authors studied the spatial evolution of the two form parameters in the case of long-crested JONSWAP random waves propagating over a shoal. They found that the surface elevation has a local minimum of skewness some distance into the down slope of the lee side of the shoal. However, a local maximum was found some distance inside the shallower side of the shoal. The authors also demonstrated that the locations of the maxima of skewness and kurtosis seemingly coincide. Moreover, experimental [24] and numerical studies [25,26] have investigated the spatial evolution of the skewness and kurtosis in the case of constant wave steepness (CWS) wave trains ([24]) and obtained qualitatively similar results to those found in [20,23].

Skewness and kurtosis are of great importance for navigation and coastal applications. The prediction of these parameters can be obtained numerically [27,28]. However, most of the existing wave models are used in the open seas (i.e., deep-water locations) and exhibit a low resolution in the nearshore zone. Considering the rapid advancement in the wave forecasting field, machine learning (ML) comes into play to offer a wealth of techniques to extract information from data that can then be translated into knowledge [29–31]. Among various machine learning algorithms, the Multilayer perceptron (MLP) algorithm [32,33] is selected in this study for kurtosis forecasting. MLP is a supervised learning algorithm that provides powerful information processing based on nonlinear regression by optimizing the squared error. The spatial evolution of the kurtosis parameter is a nonlinear problem; thus, linear regression is not suitable for this application, and it is for that reason that MLP was selected. Input datasets of the MLP included wave nonlinearity, abscissa along the flume and experimental kurtosis values. The framework is based on the Python library Scikit-Learn version 0.21.3.

2. Materials and Methods

Details of the experiments are presented in [15]. However, for the completeness of this study, a brief introduction of the generation of breaking wave trains and surface elevation measurements is provided below. The experiments were conducted in a two-dimensional wave flume at the Laboratory of M2C, Caen. The wave flume was 20 m long, 0.8 m wide,

and filled with tap water to a depth of $h_0 = 0.3$ m. A piston type wavemaker was located at one end of the flume to generate the wave trains, and an absorber beach was placed at the opposite end to help damp the incident waves. Temporal variation in surface elevations at desired locations along the wave flume was recorded by wave gauges, along with a high-speed camera. Two wave gauges were arranged to measure the free surface elevations at fifty pre-setting locations along the wave flume. The first wave gauge WG1 was located 4 m away from the wavemaker in order to measure the input wave parameters. The sampling rate for the wave gauges was 50 Hz. In our experiments, only one wave group was generated in each test, and the duration of the data acquisition was 35 s. Temporal surface elevation measurements were used to examine the maximum wave height H_m , the significant wave height H_s , the spectral bandwidth v , the skewness λ_3 and the kurtosis λ_4 along the flat and the sloping beach, which had an angle of $\alpha = 1/25$ (Figure 1).

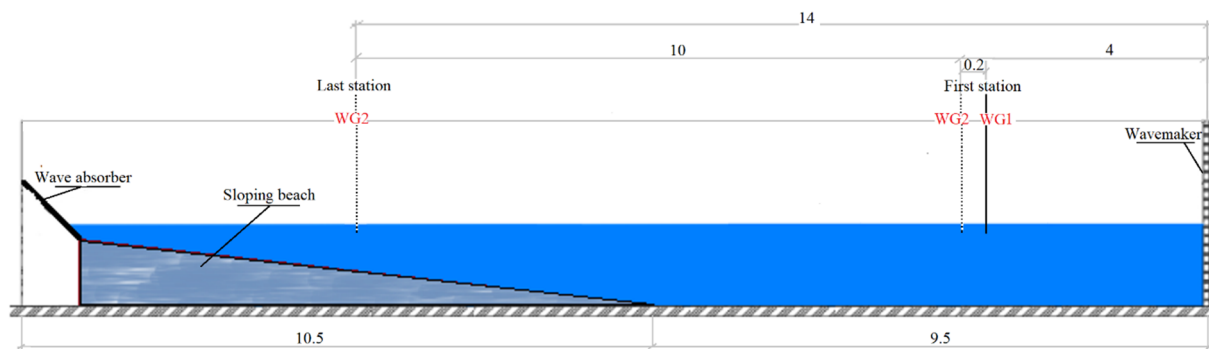


Figure 1. Experimental set-up. WG1 and WG2 are, respectively, wave gauge 1 and wave gauge 2. $x = 0$ is defined as the mean position of the wavemaker.

Preliminary tests were made in order to investigate the repeatability. Surface elevation measurements at the same location were conducted. Before breaking, differences were less than 2% (in order of error of the measurements). However, tests are less repeatable once the wave train breaks due to the entrapped compressed air present during the breaking process. Consequently, we are confident that our experiments are sufficiently repeatable.

The wave trains were generated by imposing an input wave spectrum at the wave-maker. The energy distribution in the frequency domain is defined by the JONSWAP ($\gamma = 3.3$ and $\gamma = 7$) and the Pierson–Moskowitz spectra with peak frequency varying between $f_p = 0.66$ Hz and $f_p = 0.75$ Hz, which means that $k_p h_0$ ranges between 0.8 and 0.93. This implies that the wave trains start propagating in intermediate water depths ($k_p h_0 > 0.5$). The steepness parameter $S_0 = k_{S0} \sum_{i=1}^N a_i$, the same as the local wave steepness adopted in [15], and a modified version of the Benjamin–Feir Index (BFI) (Equation (1)), which measures the ratio of the wave steepness to the spectral bandwidth in a finite water depth [34], are used to characterize wave trains.

$$BFI = \sqrt{2} \frac{k_p S_0}{v} \quad (1)$$

Here, k_p is the wavenumber related to the pic frequency f_p and calculated using the linear finite water depth relation; $\sum_{i=1}^N a_i$ is the surface elevation at the focusing location according to linear wave theory; k_{S0} is the spectrally weighted wavenumber calculated at $x = 4$ m from the wavemaker; and v is the spectral bandwidth, which is calculated using the definition given by [35] limited to wave groups with narrow-banded random sea-states:

$$v = \sqrt{\frac{m_0 m_2}{m_1^2} - 1} \quad (2)$$

Here, m_i is the i^{th} spectral moment, calculated as follows:

$$m_i = \int_{f_{min}}^{f_{max}} (2\pi f)^i S(f) df \quad (3)$$

where $S(f)$ is the frequency spectrum. Longuet-Higgins [35] recommended imposing low and high cut-off frequencies in the case of broad-banded wave trains to calculate the i^{th} spectral moment. In this study, $f_{min} = 0.3$ Hz and $f_{max} = 3$ Hz are, respectively, the lower and the upper cut-off frequencies. Figure 2 shows the spatial evolution of the spectral broadening of the studied wave trains, which is mainly related to the increasing trend of the spectral energy in high-frequency components, demonstrated in [15]. Generally, the initial spectral bandwidth is higher than 0.25 Hz; therefore, wave trains are considered as relatively broad-banded waves. Most of the generated wave trains in this study have more than one breaker, and so breaking locations (x_b) are presented as intervals. Table 1 presents some key parameters of the generated wave trains, which are categorized via their spectrum type, their nonlinearity S_0 and their BFI parameter. Twelve selected tests with different spectra and steepness, taken from [15], are studied. Segments of the measured free surface elevation of WTJ3 at six different locations along the wave flume are shown in Figure 3.

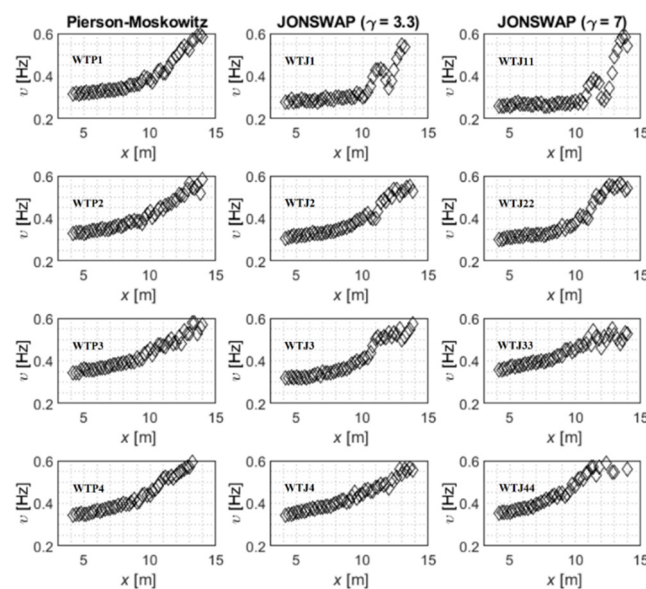


Figure 2. The spatial evolution of the spectral broadening v .

Skewness, λ_3 (Equation (4)), is a statistical parameter that is contributed to primarily by the second-order nonlinear interactions between bound waves, and kurtosis, λ_4 (Equation (5)), is a statistical parameter that includes a dynamic component due to the third-order interactions between wave components. The latter parameter indicates whether the probability density of a surface elevation's peak is higher or lower than that of a typical Gaussian distribution [25]. The kurtosis increase may indicate the formation of extreme waves [26]. In other words, kurtosis measures the weight of the peak relative to the rest of the distribution. In the case of a Gaussian sea state, $\lambda_3 = 0$ and $\lambda_4 = 0$ are normally expected. However, for a non-Gaussian sea state, $\lambda_3 > 0$ is related to sharper crests and troughs, whereas $\lambda_3 < 0$ is related to wider crests and troughs. Moreover, $\lambda_4 > 0$ is related to an increased probability of the occurrence of extreme waves. In this paper, excess kurtosis (Equation (5)) is used instead of kurtosis [36].

$$\lambda_3 = N^{1/2} \frac{\sum_{i=1}^N (\eta_i - \bar{\eta})^3}{(\sum_{i=1}^N (\eta_i - \bar{\eta})^2)^{3/2}} \quad (4)$$

$$\lambda_4 = N \frac{\sum_{i=1}^N (\eta_i - \bar{\eta}_i)^4}{(\sum_{i=1}^N (\eta_i - \bar{\eta}_i)^2)^2} - 3 \quad (5)$$

In Equations (4) and (5), N is the number of samples used in the calculation. The number of samples should be carefully chosen because this may have an impact on the magnitude of the calculated skewness and kurtosis. No null values of $\eta(t)$ are included in the calculation of skewness and kurtosis; i.e., only the part of the measurement whose value is greater than one-fiftieth is included. The mean value of sea surface is $\bar{\eta}_i \sim 0$.

Table 1. Wave train key parameters. γ is the peak enhancement factor. It is the ratio of the maximum spectral energy to the maximum of the corresponding Pierson–Moskowitz spectrum. The lower value $\gamma = 3.3$ corresponds to the standard JONSWAP formulation, and $\gamma = 7$ provides a narrower spectrum.

Wave Train	Spectrum	S_0	BFI	$h_0 k_p$	Breaking Location [m]
WTP1	Pierson–Moskowitz	0.19	2.27	0.8	[12.69,13.28]
WTP2	Pierson–Moskowitz	0.23	2.61	0.8	[12.18,12.67]
WTP3	Pierson–Moskowitz	0.28	3.05	0.8	[11.09,11.82]
WTP4	Pierson–Moskowitz	0.29	3.15	0.8	[11.02,11.89]
WTJ1	JONSWAP ($\gamma = 3.3$)	0.16	2.54	0.93	[12.9,13.7]
WTJ2	JONSWAP ($\gamma = 3.3$)	0.25	3.57	0.93	[12.13,12.81]
WTJ3	JONSWAP ($\gamma = 3.3$)	0.26	3.55	0.93	[12.07,12.76]
WTJ4	JONSWAP ($\gamma = 3.3$)	0.36	4.57	0.93	[11,11.96]
WTJ11	JONSWAP ($\gamma = 7$)	0.11	1.86	0.93	13.5
WTJ22	JONSWAP ($\gamma = 7$)	0.23	3.23	0.93	[12.07,12.69]
WTJ33	JONSWAP ($\gamma = 7$)	0.27	3.32	0.93	[11.95,12.49]
WTJ44	JONSWAP ($\gamma = 7$)	0.35	4.33	0.93	[10.71,11.86]

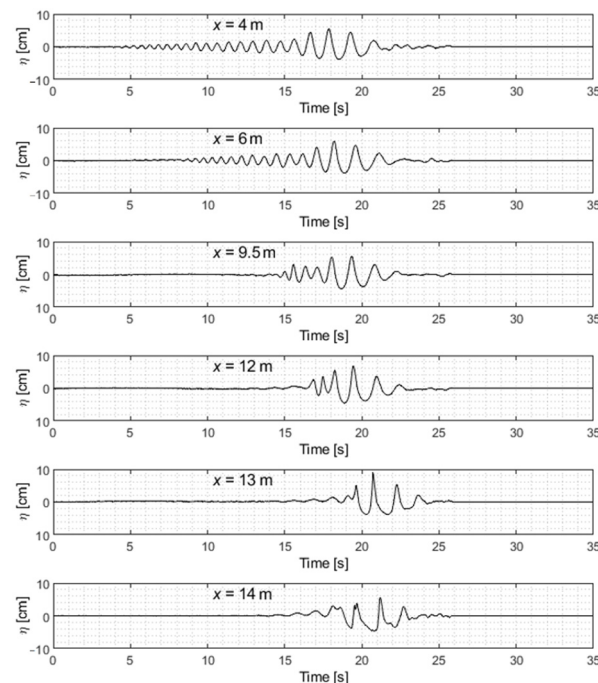


Figure 3. Segments of the surface elevations for the case WTJ3 measured at different locations along the wave flume. $x = 9.5$ m is the toe of the slope.

3. Results and Discussions

In this section, the skewness and kurtosis coefficients are experimentally estimated at different wave stations along the flume. Figures 4–6 show the spatial evolution of the two shape parameters. The two vertical solid lines added in these figures represent the breaking

zone limits, and the horizontal dashed line depicts the thresholds of a Gaussian sea state. Generally, both kurtosis and skewness deviate substantially from the Gaussian predicted values. These deviations can be attributed to the presence of bound waves, which do not fit in with the linear dispersion relationship [18].

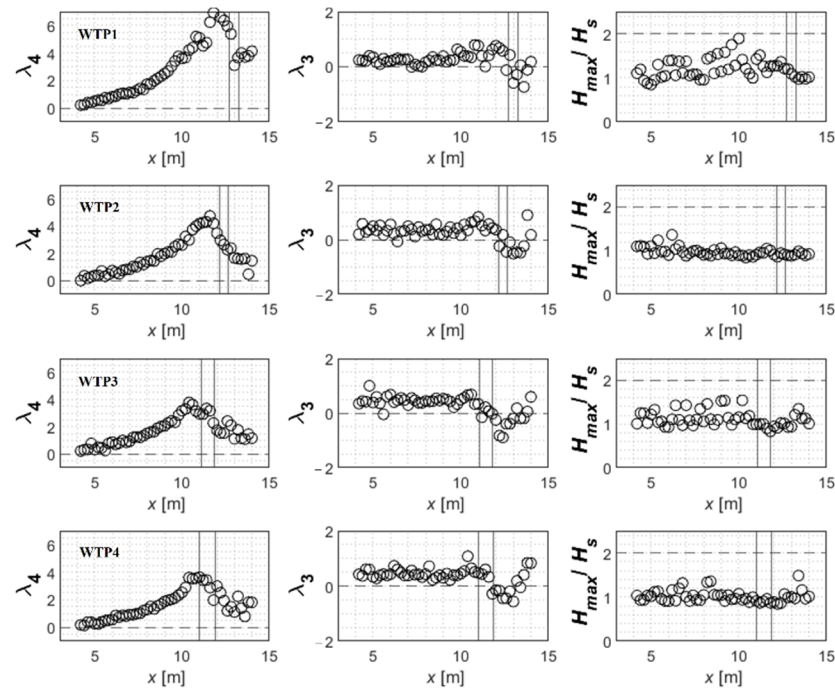


Figure 4. The spatial evolution of λ_4 , λ_3 and H_{max}/H_s for the four studied Pierson-Moskowitz wave trains.

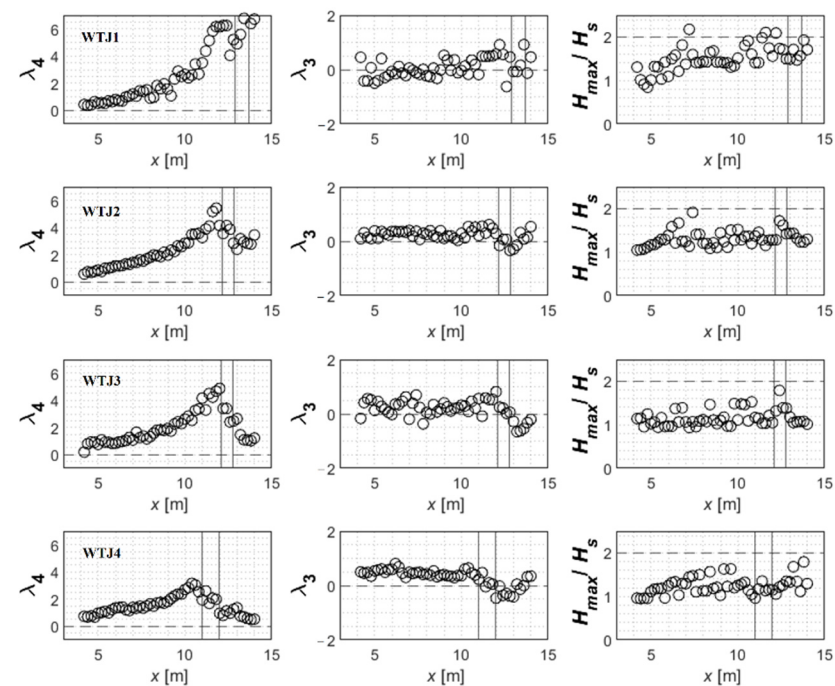


Figure 5. The spatial evolution of λ_4 , λ_3 and H_{max}/H_s for the four studied JONSWAP ($\gamma = 3.3$) wave trains.

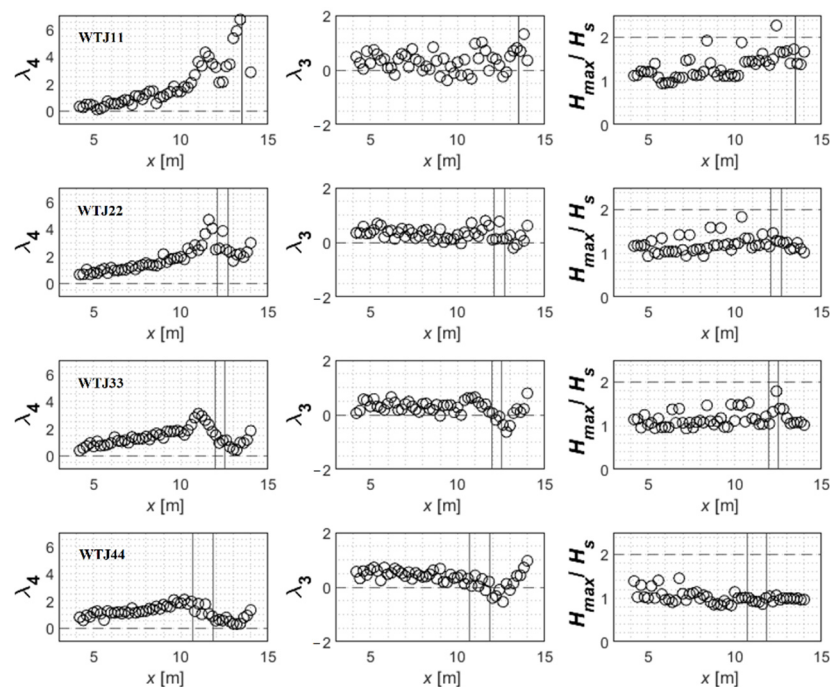


Figure 6. The spatial evolution of λ_4 , λ_3 and H_{max}/H_s for the four studied JONSWAP ($\gamma = 7$) wave trains.

When the wave train propagated on the flat bottom ($4 \text{ m} < x < 9.5 \text{ m}$), skewness $\lambda_3 \sim 0.25$ remained approximately constant, indicating a slight crest-through asymmetry for all the Pierson–Moskowitz and JONSWAP wave trains. However, kurtosis gradually increased and reached ~ 3 for both the JONSWAP and the Pierson–Moskowitz wave trains. This result is qualitatively consistent with earlier studies [23].

When the wave train reached the slope ($9.5 \text{ m} < x < x_b$), kurtosis increased rapidly, and skewness increased slightly until reaching the surf zone, where most of the high-frequency waves finish breaking. The evolution of maxima of kurtosis is shown to depend on wave nonlinearity, S_0 . In other words, the wave trains with small nonlinearities become more nonlinear during the shoaling process than those with higher nonlinearities, which break in deeper regions before undergoing notable shoaling.

The maxima of skewness and kurtosis were reached just prior to breaking ($x \sim x_b$). Tian et al. [24] made the same conclusions in the case of constant steepness in wave trains propagating in deep water conditions. Just prior to breaking, the maximum kurtosis value reached was around $\lambda_4 = 7$, which is greater than to that found in previous studies, such as in [19,20,37]. This might be explained by the sampling variability effect (See [38]). The duration of each experiment in our study is 35 s, whereas it is 20 min of continuous random JONSWAP waves in [20]. As mentioned in [24], when only one wave train is generated in each experiment, quantitative results found concerning skewness and kurtosis do not concern field measurements of continuous wave groups.

In Tian et al. [24], the maximum skewness found was less than 1. The maximum skewness obtained in our study indicates a stronger crest-trough asymmetry ($\lambda_3 > 1$). This can be explained by the shoaling phenomenon, since all the wave trains generated break on the slope. As mentioned in [20], the increase in λ_3 and λ_4 is mainly due to the second-order nonlinear interactions associated with wave shoaling and shallow water effects.

After the breaking ($x > x_b$), the wave train dispersed again and becomes less steep, and both skewness and kurtosis converged to zero. Similar conclusions were made by [1], who found that the maximum values of λ_3 and λ_4 can be obtained in the vicinity of the plunging breaker location. This may be explained by the fact that the breaking process is accompanied by an important energy dissipation, especially in high-frequency components [15]. The breaking process eliminated the strong crest-trough asymmetries, and, as a result, skewness

approached zero. Near the coast ($x > 13$ m), the wave train nonlinearity increased again when the shoaling of the low-frequency waves became more significant. This is clearly illustrated in Figures 4–6, where skewness is slightly greater than 0.

Figure 7 shows the initial and maximum values of ν , λ_3 and λ_4 as a function of the BFI parameter. Surface elevation measured at the first wave station (WG1 in Figure 1) was used to calculate the initial BFI value. However, local BFI values were calculated where the maximum spectral bandwidth, skewness and kurtosis were achieved. Generally, we found that the local BFI values were lower than the initial ones, and this is related to the spectrum broadening along the wave train propagation. The initial and maximum spectral bandwidth ν remained approximately constant with the increase in the Benjamin–Feir Index, which is in accordance with the results found in [24]. Additionally, no clear correlations between the BFI and the maximum values λ_3 and λ_4 could be identified.

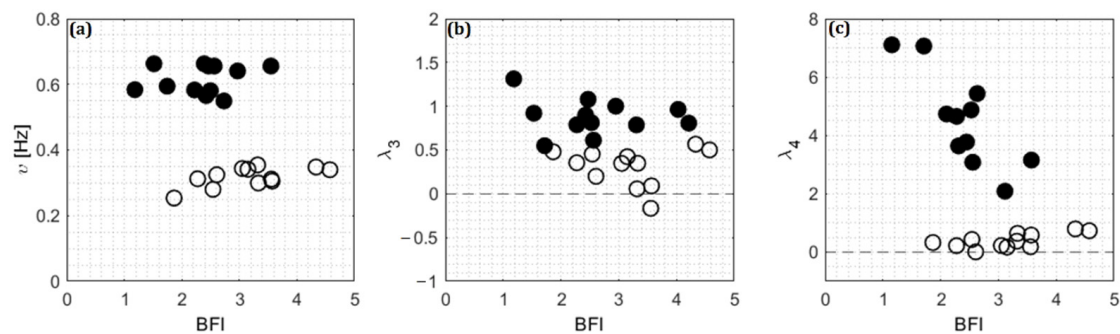


Figure 7. Dependence of spectral bandwidth, skewness and kurtosis on BFI parameter. Open symbols: (a) the initial spectral bandwidth ν , (b) the initial skewness λ_3 , (c) the initial kurtosis λ_4 . Solid symbols: (a) the maximum spectral bandwidth, (b) the maximum skewness, (c) the maximum kurtosis.

Figure 8 shows the relationship between skewness and kurtosis in intermediate and shallow water depth before and after the toe of the slope. The solid black line (Equation (6)) depicts the second-order nonlinear theory first developed by [39], reflecting the water depth change proposed by [40]. The solid blue line (Equation (7)) represents an adjusted formula introduced by the data observed in the sloping bottom. We mention here that a narrow-banded wave approximation is adopted in the second-order theory, and this theoretical model shows that the kurtosis parameter increases when skewness increases.

$$\lambda_4^{(1)} = \left(\frac{4}{3}\lambda_3\right)^2 \quad (6)$$

$$\lambda_4^{(2)} = 2 + \left(\frac{4}{3}\lambda_3\right)^2 \quad (7)$$

The experimental data on the flat and on the sloping bottom have a qualitatively similar tendency. For the data on the flat bottom, i.e., $k_p h_0 > 0.8$, the results are in qualitative agreement with the theoretical model of [40]. For the data on the sloping bottom, i.e., $k_p h_0 < 0.8$, kurtosis is underestimated by the theoretical model. As expected, most of the skewness and kurtosis values of the experimental data are underpredicted along the flume if only the second-order theory is considered. Mori et al. [18] found a better agreement between experimental data and theory when the free wave effect was included [41]. It is important to note that the formulations in [18] were obtained using numerical simulations in the case of Gaussian deep-water waves, which explains the differences in field measurements, as pointed out by [22].

Figure 9 shows the relationship between the maximum wave height H_{max}/H_s , skewness λ_3 and kurtosis λ_4 , on the flat and on the sloping bottom. The solid black curve depicts the H_{max}/H_s empirical formulae proposed by [41], and the dashed line represents the threshold of freak waves, i.e., $H_{max}/H_s = 2$. The ratio H_{max}/H_s is nearly flat between 1

and 2.5 according to the incident wave steepness, although kurtosis and skewness rapidly increased under the effects of the second-order nonlinear interactions due to the shoaling phenomenon. Consequently, the dependence between H_{max}/H_s and the two form parameters is weak in shallow water locations.

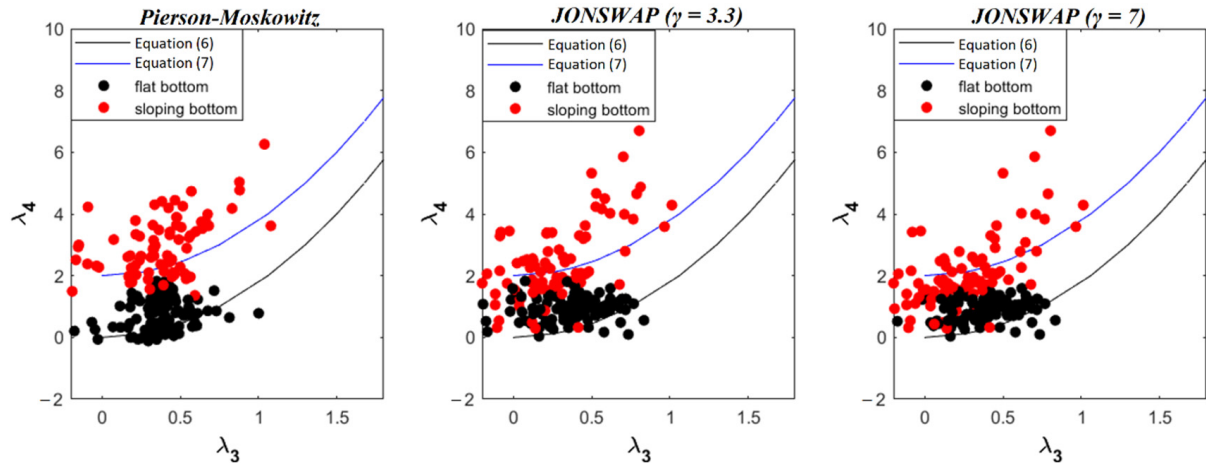


Figure 8. Relationship between skewness and kurtosis from intermediate to shallow water regions before and after the toe of the slope. The solid black line represents the second-order nonlinear theory with respect to water depth change [40]. The solid blue line depicts an adjusted formula introduced by the data found in the sloping bottom.

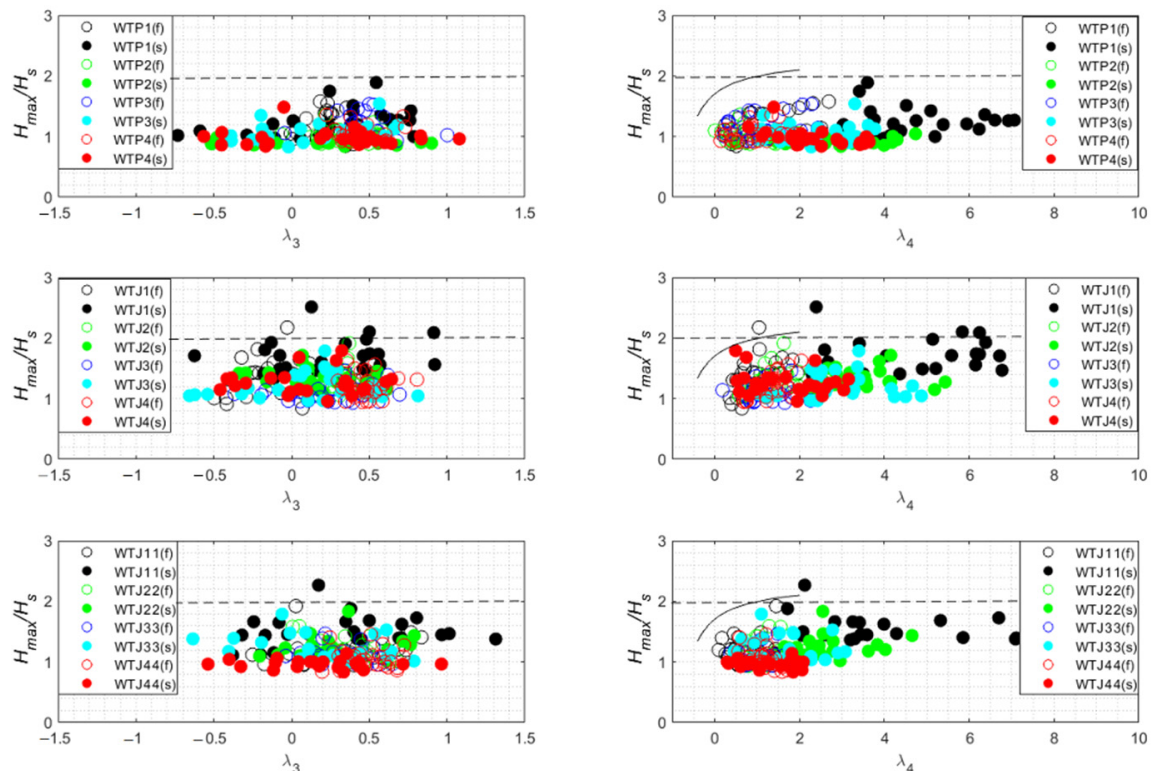


Figure 9. Relationship between the maximum wave height H_{max}/H_s , skewness λ_3 and kurtosis λ_4 on the flat and on the sloping bottom. Empty circles represent the flat bottom data (f) and filled circles exhibit the sloping bottom data (s). The solid black curve depicts the H_{max}/H_s empirical formulae proposed by [41].

Lastly, we tested the MLP algorithm in order to predict the spatial evolution of the kurtosis parameter. Figure 10 shows that the kurtosis predictions are satisfactory, and the

accuracy score is around 0.88 for the Pierson–Moskowitz wave trains, 0.9 for JONSWAP ($\gamma = 3.3$) and 0.8 for JONSWAP ($\gamma = 7$). To gain a better understanding, more data (i.e., higher and lower nonlinearities) should be investigated. Aside from the intense data requirement, sensitivity tests on hyperparameters, such as the stepsize (α) and the exponential decay rates for momentum estimates (β_1 , β_2), should be performed in order to achieve a more accurate MLP model.

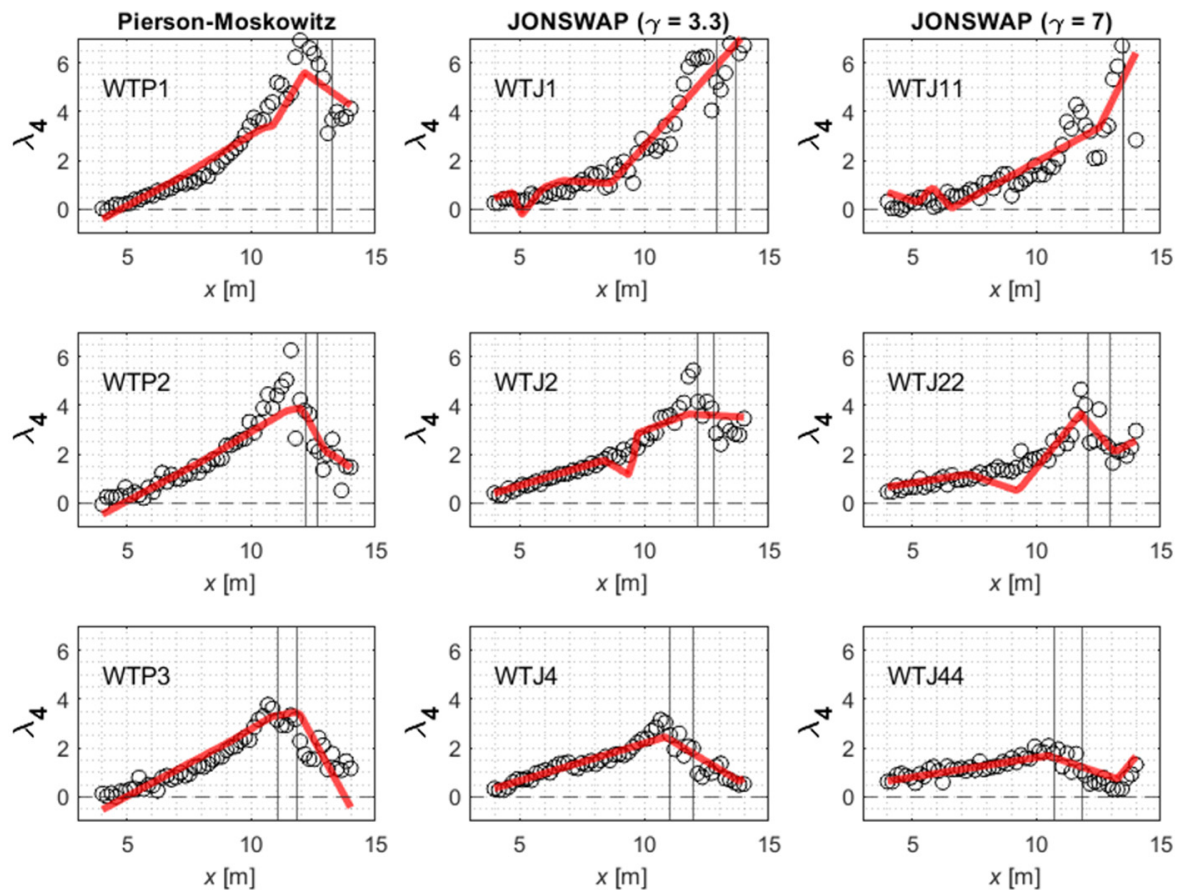


Figure 10. Experimental (open circles) versus predicted (red continuous line) values of kurtosis.

4. Conclusions and Perspectives

The presence of extreme wave events can contribute to the significant deviations in the Gaussian sea state model and the Rayleigh statistics. The present study aimed to investigate the spatial evolution of maximum wave heights, skewness and kurtosis. Using the dispersive focusing technique, group focused waves derived from three different spectra (Pierson–Moskowitz, JONSWAP ($\gamma = 3.3$ and $\gamma = 7$)) and with the different breaking intensities were generated in the laboratory flume.

Generally, the skewness and the kurtosis for the JONSWAP and the Pierson–Moskowitz wave trains are qualitatively quite similar. Above the flat bottom ($4 \text{ m} < x < 9.5 \text{ m}$), we found that skewness remained approximately constant; however, kurtosis increased gradually during the wave train propagation over the range of conducted tests. Moreover, the skewness and kurtosis magnitudes along this portion of the flume depended on the wave steepness. This is illustrated in Figures 4–6, where the skewness values are slightly higher in the case of strong nonlinearities, S_0 . Nevertheless, there was a quick transition from intermediate to shallow water depth. Kurtosis depended on the evolution of skewness regardless of the incident wave steepness, (S_0). It is shown that the second-order theory, suggested by [40] (Equation (6)), fits well with the data measured along the flat bottom. When the shoaling process started, the formula clearly underestimated kurtosis, and a modified version was proposed (Equation (7)). Generally, the scatter of the data was

large, and this can be partially explained by important wave–wave interactions, which are not taken into account in the second-order theory. Furthermore, we found that the ratio H_{max}/H_s was constant, although the two form parameters increased rapidly in shallow regions. Therefore, the link between H_{max}/H_s and the two form parameters was very weak in shallow water regions in the case of our experiments.

Due to the randomness of the Pierson–Moskowitz and the JONSWAP spectra, wave statistics will depend on which portion of a record is used in the analysis. In other words, the length of a wave recorded in the investigated wave train is very important. An inherent disadvantage of this study is the problem of sampling variability. This kind of problem can be addressed by increasing the duration of temporal measurements in order to provide accurate form parameters and to quantify the effects of the sampling variability.

A machine learning MLP algorithm was used in order to predict the spatial evolution of kurtosis. We found that this MLP algorithm was able to identify patterns and to reproduce the spatial evolution of kurtosis in a satisfactory manner. This study shows that the MLP algorithm is a promising tool for improving wave forecasting in field measurements and that it can accelerate kurtosis spatial evolution forecasting while retaining good predictive accuracy. In the near future, we plan to perform new tests involving lower and higher wave steepness in order to extend simulations to wider wave train spectra and to improve the prediction of the spatial evolution of extreme wave statistics using the MLP machine learning algorithm.

Supplementary Materials: The following supporting information can be downloaded at: <https://www.mdpi.com/article/10.3390/jmse10101475/s1>.

Author Contributions: Conceptualization, I.A.; methodology, I.A.; investigation, I.A.; resources, I.A.; data curation, I.A.; writing—original draft preparation, I.A. and R.M.; writing—review and editing, I.A. and N.A.; visualization, I.A.; supervision, N.A.; project administration, N.A.; funding acquisition, N.A. All authors have read and agreed to the published version of the manuscript.

Funding: This research received no external funding.

Institutional Review Board Statement: Not applicable.

Informed Consent Statement: Not applicable.

Data Availability Statement: The free surface elevations files of the twelve wave trains are available in the Supplementary Materials.

Acknowledgments: The authors wish to express their gratitude to Sonia Baatout for her thorough re-reading of this article. The authors would like also to express their gratitude to the referees who helped us to improve our manuscript quality.

Conflicts of Interest: The authors declare no conflict of interest.

References

1. Bitner, E.M. Non-linear effects of the statistical model of shallow-water wind waves. *Appl. Ocean Res.* **1980**, *2*, 63–73. [\[CrossRef\]](#)
2. Kharif, C.; Pelinovsky, E. Physical mechanisms of the rogue wave phenomenon. *Eur. J. Mech. B Fluids* **2003**, *22*, 603–635. [\[CrossRef\]](#)
3. Gao, J.; Ma, X.; Zang, J.; Dong, G.; Ma, X.; Zhu, Y.; Zhou, L. Numerical investigation of harbor oscillations induced by focused transient wave groups. *Coast. Eng.* **2020**, *158*, 103670. [\[CrossRef\]](#)
4. Gao, J.; Chen, H.; Zang, J.; Chen, L.; Wang, G.; Zhu, Y. Numerical investigations of gap resonance excited by focused transient wave groups. *Ocean Eng.* **2020**, *212*, 107628. [\[CrossRef\]](#)
5. Whittaker, C.N.; Fitzgerald, C.J.; Raby, A.C.; Taylor, P.H.; Borthwick, A.G.L. Extreme coastal responses using focused wave groups: Overtopping and horizontal forces exerted on an inclined seawall. *Coast. Eng.* **2018**, *140*, 292–305. [\[CrossRef\]](#)
6. Henning, J.; Schmittner, C.E. Experimental variation of focusing wave groups for the investigation of their predictability. In Proceedings of the ASME 2009 28th International Conference on Ocean, Offshore and Arctic Engineering, Honolulu, HI, USA, 31 May–5 June 2009; Volume 43468, pp. 641–651. [\[CrossRef\]](#)
7. Dean, R.G. Freak waves: A possible explanation. In *Water Wave Kinematics*; Tørum, A., Gudmestad, O.T., Eds.; Springer: Dordrecht, The Netherlands, 1990; Volume 178. [\[CrossRef\]](#)
8. Gao, J.; Ma, X.; Dong, G.; Chen, H.; Liu, Q.; Zang, J. Investigation on the effects of Bragg reflection on harbor oscillations. *Coast. Eng.* **2021**, *170*, 103977. [\[CrossRef\]](#)

9. Gao, J.L.; Chen, H.Z.; Mei, L.L.; Liu, Z.; Liu, Q. Statistical analyses of wave height distribution for multidirectional irregular waves over a sloping bottom. *China Ocean Eng.* **2021**, *35*, 504–517. [\[CrossRef\]](#)
10. Steve, E.; Guza, R.T. Observations of bispectra of shoaling surface gravity waves. *J. Fluid Mech.* **1985**, *161*, 425–448. [\[CrossRef\]](#)
11. Ma, Y.; Dong, G.; Ma, X. Experimental study of statistics of random waves propagating over a bar. *Coast. Eng. Proc.* **2014**, *1*, 34. [\[CrossRef\]](#)
12. Huang, W.; Dong, S. Statistical properties of group height and group length in combined sea states. *Coast. Eng.* **2021**, *166*, 103897. [\[CrossRef\]](#)
13. Trulsen, K.; Zeng, H.; Gramstad, O. Laboratory evidence of freak waves provoked by non-uniform bathymetry. *Phys. Fluids A* **2012**, *24*, 097101. [\[CrossRef\]](#)
14. Petrova, P.; Gueded, S.C. Maximum wave crest and height statistics of irregular and abnormal waves in an offshore basin. *Appl. Ocean Res.* **2008**, *30*, 144–152. [\[CrossRef\]](#)
15. Abroug, I.; Abcha, N.; Dutykh, D.; Jarno, A.; Marin, F. Experimental and numerical study of the propagation of focused wave groups in the nearshore zone. *Phys. Lett. A* **2020**, *6*, 126144. [\[CrossRef\]](#)
16. Abroug, I.; Abcha, N.; Jarno, A.; Marin, F. Laboratory study of non-linear wave-wave interactions of extreme focused waves in the nearshore zone. *Nat. Hazard Earth Syst.* **2020**, *20*, 3279–3291. [\[CrossRef\]](#)
17. Zhang, J.; Benoit, M.; Kimmoun, O.; Chabchoub, A.; Hsu, H.C. Statistics of extreme waves in coastal waters: Large scale experiments and advanced numerical simulations. *Fluids* **2019**, *4*, 99. [\[CrossRef\]](#)
18. Mori, N.; Onorato, M.; Janssen, P.A.E.M.; Osborne, A.R.; Serio, M. On the extreme statistics of long-crested deep-water waves: Theory and experiments. *J. Geophys. Res.* **2007**, *112*. [\[CrossRef\]](#)
19. Shemer, L.; Sergeeva, A. An experimental study of spatial evolution of statistical parameters in a unidirectional narrow-banded random wavefield. *J. Geophys. Res.* **2009**, *114*. [\[CrossRef\]](#)
20. Kashima, H.; Hirayama, K.; Mori, N. Estimation of freak wave occurrence from deep to shallow water regions. *Coast. Eng. Proc.* **2014**, *1*, 36. [\[CrossRef\]](#)
21. Vinje, T.; Haver, S. On the non-Gaussian structure of ocean waves. In Proceedings of the 7th International Conference on the Behaviour of Offshore Structures, Cambridge, MA, USA, 12–15 July 1994; Pergamon Press: Oxford, UK, 1994; Volume 5, p. 435.
22. Bitner-Gregersen, E.M.; Gramstad, O. Comparison of temporal and spatial statistics of nonlinear waves. In Proceedings of the ASME 2019 38th International Conference on Ocean, Offshore and Arctic Engineering, Glasgow, UK, 9–14 June 2019; p. 3.
23. Trulsen, K.; Raustøl, A.; Jorde, S.; Bæverfjord, R. Extreme wave statistics of long-crested irregular waves over a shoal. *J. Fluid Mech.* **2019**, *882*, R2. [\[CrossRef\]](#)
24. Tian, Z.; Perlin, M.; Choi, W. Frequency spectra evolution of two-dimensional focusing wave groups in finite depth water. *J. Fluid Mech.* **2011**, *688*, 169–194. [\[CrossRef\]](#)
25. Zeng, H.; Trulsen, K. Evolution of skewness and kurtosis of weakly nonlinear unidirectional waves over a sloping bottom. *Nat. Hazards Earth Syst.* **2012**, *12*, 631–638. [\[CrossRef\]](#)
26. Mori, N.; Onorato, M.; Janssen, P.A.E.M. On the estimation of the kurtosis in directional sea states for freak wave forecasting. *J. Phys. Oceanogr.* **2011**, *41*, 1484–1497. [\[CrossRef\]](#)
27. Toffoli, A.; Onorato, M.; Bitner-gregersen, E.; Osborne, A.R.; Babanin, A.V. Surface gravity waves from direct numerical simulations of the Euler equations: A comparison with second-order theory. *Ocean Eng.* **2008**, *35*, 367–379. [\[CrossRef\]](#)
28. Toffoli, A.; Benoit, M.; Onorato, M.; Bitner-gregersen, E. The effect of third-order nonlinearity on statistical properties of random directional waves in finite depth. *Nonlinear Process. Geophys.* **2009**, *16*, 131–139. [\[CrossRef\]](#)
29. Günaydin, K. The estimation of monthly mean significant wave heights by using artificial neural network and regression methods. *Ocean Eng.* **2008**, *35*, 1406–1415. [\[CrossRef\]](#)
30. Malekmohamadi, I.; Bazargan-Lari, M.R.; Kerachian, R.; Nikoo, M.R.; Fallahnia, M. Evaluating the efficacy of SVMs, BNs, ANNs and ANFIS in wave height prediction. *Ocean Eng.* **2011**, *38*, 487–497. [\[CrossRef\]](#)
31. James, S.C.; Zhang, Y.; O'Donncha, F. A machine learning framework to forecast wave conditions. *Coast. Eng.* **2018**, *137*, 1–10. [\[CrossRef\]](#)
32. White, H.; Gallant, A.R.; Hornik, K.; Stinchcombe, M.; Wooldridge, J. *Artificial Neural Networks: Approximation and Learning Theory*; Basil Blackwell: Oxford, UK, 1992. [\[CrossRef\]](#)
33. Rynkiewicz, J. General bound of overfitting for MLP regression models. *Neurocomputing* **2012**, *90*, 106–110. [\[CrossRef\]](#)
34. Dutykh, D. Evolution of random wave fields in the water of finite depth. *Procedia IUTAM* **2014**, *11*, 34–43. [\[CrossRef\]](#)
35. Longuet-Higgins, M.S. Statistical properties of wave groups in a random sea state. *Phil. Trans. R. Soc. Lond. A* **1984**, *312*, 219–250. [\[CrossRef\]](#)
36. Janssen, P.A.E.M. On some consequences of the canonical transformation in the Hamiltonian theory of water waves. *J. Fluid Mech.* **2009**, *637*, 1–44. [\[CrossRef\]](#)
37. Onorato, M.; Cavaleri, L.; Fouques, S.; Gramstad, O.; Janssen, P.A.E.M.; Monbaliu, J.; Osborne, A.R.; Pakozdi, C.; Serio, M.; Stansberg, C.T.; et al. Statistical properties of mechanically generated surface gravity waves: A laboratory experiment in a three-dimensional wave basin. *J. Fluid Mech.* **2009**, *627*, 235–257. [\[CrossRef\]](#)
38. Bitner-Gregersen, E.M.; Gramstad, O.; Magnusson, A.K.; Malila, M.P. Extreme wave events and sampling variability. *Ocean Dyn.* **2020**, *71*, 81–95. [\[CrossRef\]](#)

39. Longuet-Higgins, M.S. The effect of non-linearities on statistical distributions in the theory of sea waves. *J. Fluid Mech.* **1963**, *17*, 459. [[CrossRef](#)]
40. Mori, N.; Kobayashi, N. Nonlinear distribution of nearshore free surface and velocity. In Proceedings of the 26th International Conference of Coastal Engineering, Copenhagen, Denmark, 22–26 June 1998; Volume 1, pp. 189–202. [[CrossRef](#)]
41. Janssen, P.A.E.M. Nonlinear four-wave interactions and freak waves. *J. Phys. Oceanogr.* **2003**, *33*, 2001–2018. [[CrossRef](#)]